Subsurface temperature from seismic reflections: application to the post break up sequence offshore Namibia

Arka Dyuti Sarkar[1] (arkadyuti.sarkar@manchester.ac.uk) – *Corresponding author*

Mads Huuse[1] (mads.huuse@manchester.ac.uk)

[1]Department of Earth and Environmental Sciences, The University of Manchester, Williamson Building, Oxford Road, Manchester, M13 9PL.

Acknowledgements

The authors would like to thank Serica Energy and Spectrum ASA (now TGS) for provision of seismic data utilised as part of this research. We would like to thank Schlumberger for the provision of the Petrel licenses. The authors would like to thank two anonymous reviewers and editor Robert Merrill for their feedback and comments that helped improve the quality of the manuscript. We would also like to thank Kofi Owusu, Andrew Newton, David Hodgetts, and Benedict Campbell for their assistance with key sections of the project. Thanks also go to ADS's parents for their generous funding of his research.

Abstract

Accurate estimations of present-day subsurface temperatures are of critical importance to the energy industry, in particular with regards to geothermal energy and petroleum exploration. In frontier basins, the subsurface temperature regime can give an indication of the hydrocarbon potential of source horizons. The Lüderitz Basin, offshore Namibia, is a

frontier deep water basin located on a volcanic passive margin. With only two wells drilled in the area, there are limited downhole temperature data available with which to constrain the hydrocarbon window of key source rock intervals. However, high quality seismic data are available and, by applying the reflection seismic thermometry (RST) process, provides a remote sensing alternative to direct temperature measurements at high spatial resolution. Using seismic reflection and velocity data, firstly the identification of a gas hydrate bottom simulating reflector is used to derive a shallow heat flow proxy (averaging 64 mW m^{-2}). Deriving subsurface thermal conductivity from velocity data using an empirical relationship, a prediction for subsurface temperature can be made through forward modelling. Results indicate that average temperatures at the base of the Aptian Kudu Shale interval are 134 °C, placing the source in the gas generative window within the study area. This case study demonstrates the power of RST to generate indicative subsurface temperature results in frontier exploration basins, thereby reducing uncertainty over source rock maturity prior to drilling.

Introduction

Subsurface temperature is a key parameter in subsurface energy extraction from petroleum- and geothermal systems (Harper, 1971; Thompson, 1979; Hunt, 1984; Bonté et al., 2012). Accurate estimations of present-day subsurface temperatures are thus of critical importance to the energy industry. In frontier areas, petroleum source rock maturity is a key uncertainty and without access to bottom hole temperature (BHT) readings from boreholes, source rock characterisation is reliant on estimation and extrapolation. A crucial component of understanding the subsurface temperature field is how heat is transferred (i.e. heat flow and thermal conductivity) (Sclater et al., 1980). Often there is limited understanding of the

variation in thermal conductivity both vertically and laterally in the subsurface domain due to the difficulty collecting such data. Prior to entry into frontier basins, it is advantageous to determine the generative potential of the source rock in the area. This is primarily controlled by two factors namely source rock type and temperature history. Specifically, source rock type refers to the organic matter type (marine or terrestrial), the richness of the organic matter and the content (Magoon and Dow, 1994; McCarthy et al., 2011). Source rock quality and therefore petroleum prospectivity in a basin may be ascertained through geochemical analyses such as fingerprinting for key biomarkers from oil seeps for example (Burton et al., 2018, 2019). The temperature and pressure conditions that the organic matter is subjected to, as well as the duration of temperature and pressure exposure, govern the degree of biodegradation into varying types of hydrocarbons. Along many passive margins the source rocks are at maximum burial depth and thus maximum temperature at the present day. Present day subsurface temperatures are typically acquired from temperature probe measurements that have been acquired in boreholes(Fuchs and Balling, 2016). To estimate heat flow and temperature information in adjacent areas often involves the deployment of multiple seafloor probes prior to the drilling stage (Davis et al., 2003). This then requires the extrapolation of data from nearby boreholes using structural and stratigraphic models (Davies and Davies, 2010). This methodology underutilises the available seismic datasets that are often acquired during the early stages of exploration in frontier basins. This paper presents a reflection seismic thermometry (RST) workflow for using seismic reflection data to estimate subsurface temperature before drilling and applies this to a frontier exploration setting.

It has been shown that gas hydrate identification on seismic reflection data through detection of bottom simulating reflectors (BSRs) at the base of gas hydrate stability zone (GHSZ), can be

71 used for geothermal gradient estimation (Yamano et al., 1982; Calvès et al., 2010; Hodgson
72 et al., 2014; Serié et al., 2017).

73 RST predicts subsurface temperatures by first estimating surface heat flow from BSRs and
74 then utilizing seismic processing velocities to derive thermal conductivity through an
75 empirical transform. This empirical relationship relating acoustic velocity and thermal
76 conductivity is a key component in allowing the estimation of subsurface temperatures
77 throughout the seismic volume.

78 **Figure 1**

79 *Geological setting*

80 The study area (Fig. 1) is in the Lüderitz Basin offshore Namibia, bounded by the Orange Basin
81 to the south, and the Walvis Basin to the north. It is part of the southern West African
82 continental margin. Successive rifting events from the Carboniferous onwards preceded the
83 Mesozoic opening of the South Atlantic, and the breakup of Gondwana (Bagguley and Prosser,
84 1999; Karner and Driscoll, 1999; Schmidt, 2004). The margin offshore Namibia is characterised
85 as having characteristics of both volcanic passive margin and non-volcanic margin end
86 members (Light et al., 1993; Gladczenko et al., 1998; Bauer et al., 2000). Asymmetric rifting
87 has resulted in significant variability in the sedimentary and subsidence history between the
88 conjugate margins with this reflected in the nature of hydrocarbons discovered in these areas
89 (Mello et al., 2011). The formation of the Walvis Ridge is contemporaneous with the extrusion
90 of the Etendeka continental flood basalts and acted as a long-lived barrier to marine flow,
91 creating restricted marine conditions to the north. These conditions promoted the formation
92 of salt basins north of the Ridge in the Albian-Aptian, and these are observed on both the
93 West African and Brazilian margins (Berger et al., 1998; Davison et al., 2012). In the Lüderitz

Basin multiple features such as seaward dipping reflectors (SDRs) and mass transport deposits (MTDs) can be observed (Torsvik et al., 2009) (Fig. 2 b,c). There are however no seamounts within 50 km (~31.1 mi) from the study area, the outer limit for hydrothermal systems to extend from such a system (Sclater et al., 1980; Hasterok et al., 2011).

The neighbouring Orange and Walvis Basins both possess working petroleum systems with gas condensate discovered in the Kudu wells and oil in the Wingat well respectively (Fig. 1) (Intawong et al., 2015). The key source interval relevant for the Lüderitz Basin is the Aptian age Kudu shale (Fig. 2). The source maturity of this interval in the Lüderitz Basin is as yet uncertain.

Figure 2

Gas Hydrates & Bottom Simulating Reflectors

A BSR is traditionally considered as a continuous and coherent seismic event that cross-cuts the primary sedimentary features, whilst mimicking the morphology of the seabed (Calvès et al., 2008; Le et al., 2015; Ruppel and Kessler, 2017; Schicks, 2018). A BSR with reverse polarity and near-parallelism relative to the seabed originates from the negative acoustic impedance (AI) contrast between partially frozen, gas-hydrate bearing sediment at the base of the GHSZ and the underlying zone of dissociated free gas and water bearing sediment (Kvenvolden & Lorenson, 2001; Paganoni et al., 2016). This variant of a BSR has been commonly noted in studies globally and is usually considered a sign of hydrate presence (Shipley and Houston, 1979; Stoll and Bryan, 1979; Haacke et al., 2007).

Heat Flow

Understanding heat flow is crucial to building reliable geological models of both the shallow and deep subsurface and has important implications for the exploration and development of natural resources such as petroleum (Tissot et al., 1987). Heat flow has traditionally been associated with tectonism and the thickness of the radiogenic crust. However, mantle processes in continental margins also impact heat flow (Goutorbe et al., 2011). Heat from the mantle or primordial heat is one contributing factor to the thermal structure in sedimentary basins and is the deepest source of heat production (Hokstad et al., 2017). Mantle heat flow is estimated from the base of the crust, equivalent to the Moho (thus the prevalence of the 1330 °C (2426 °F) isotherm as a reference point in traditional bottom-up basin modelling workflows). The other contribution to heat is in the form of radiogenic heat production. Radiogenic elements are found in insignificant quantities in oceanic crust and lithospheric

126 mantle, therefore the radiogenic heat input will be greatest in areas of continental crust and
127 sediments (Hasterok, 2010; Allen and Allen, 2013). Basins located in the transitional zone
128 between onshore and offshore regions tend to have considerable structural variability and
129 thus as a consequence have been the least predictable for heat flow using global averages
130 only (Jaupart et al., 2016; Hokstad et al., 2017). Though young ocean crust is particularly
131 susceptible to hydrothermal fluid circulation impacting heat flow, in the Lüderitz Basin this is
132 not an issue due to the relative age of the underlying crust and proximity to the coast parallel
133 continent ocean boundary (COB) (Lister, 1972; Gladczenko et al., 1998).
134 Global coverage of heat flow data is not extensive, with surface heat flow data globally being
135 limited relative to estimates of total heat output (Gosnold & Panda, 2002; Lucazeau, 2019;
136 Macgregor, 2020). In the study area, the solitary heat flow data point is from Ocean Drilling
137 Program (ODP) Site 1084 as shown in Fig. 1. Reported values of heat flow in published
138 literature are made either through direct measurement or through estimations based on
139 crustal thickness and age (Davies and Davies, 2010; Davies, 2013). Such heat flow estimates
140 can have a threefold basis with primary data from measured data points; in oceanic crustal
141 settings, heat flow is based on crustal thickness to mitigate for measurement perturbation
142 due to fluid flow; and finally in the absence of measurements an estimate can be made on
143 the basis of geology. The Bullard method is commonly used to calculate heat flow from
144 borehole data from the relation between temperature and the thermal resistance of the
145 sediments (Bullard, 1939; Pribnow et al., 2000). For there to be a linear relationship between
146 acoustic velocity and thermal conductivity conditions downhole must be conductive, steady
147 state and with no internal heat sources. The latter is difficult as heat is introduced into the
148 system during drilling from friction with the drill bit and the circulation of drilling fluids, thus
149 necessitating time-based corrections for the impact of drilling on local thermal regime.

Conventional thermal data

Over large regions like continental margins, it is difficult to ensure high spatial resolution of thermal data from conventional techniques such as downhole temperature measurements and gravity driven thermal probes (Phrampus et al., 2017). This is both a result of scarcity of boreholes and prohibitive expense. Heat flow derived from the seismic imaging of gas hydrates can be useful in areas where significant bottom water temperature (BWT) fluctuation adversely affects the reliability of thermal probe data or where hard ground may prevent probe insertion (Hyndman et al., 2001). ODP thermal conductivity measurements on core samples from gas hydrate provinces are unreliable due to gas exsolution during recovery (Phrampus et al., 2017). This phenomenon depresses onboard thermal conductivity measurements. For the transient line source needle probe used in ODP studies to measure thermal conductivity it is important to note the orientation of the needle insertion relative to the sediment bedding direction as the thermal conductivity measurement is provided for a plane perpendicular to the needle axis (Pribnow et al., 2000). For shipboard temperature measurements temperature-time curves are subjectively fit to APC probe data (to restore to equilibrium temperatures and negate the effect of frictional heating upon insertion of the probe) (Grevemeyer and Villinger, 2001).

The Curie isotherm is a common subsurface thermal marker sometimes representing a petrophysical boundary (Langel and Hinze, 1998). It is commonly considered to be ~580 °C (~ 1076 °F) as this is the Curie Point temperature of magnetite, the most common magnetic mineral in the continental crust, especially in deeper regions (Frost and Shive, 1986). Thus, the depth corresponding to a lack of magnetism is likely at temperatures in excess of the Curie point of magnetite or a result of compositional changes leading to magnetite poor rocks at

depth (Beardsmore and Cull, 2001). However, this method simply defines a solitary subsurface isotherm over a great depth interval from the seabed, thus making any linear geothermal gradient calculated greatly simplified. Furthermore, for high resolution estimation of the Curie isotherm depth, regional scale magnetic data would be required.

Global thermal data coverage may also suffer from spatial bias (for example, shelf vs deep water settings), as there tends to be a greater interest for scientists in areas of higher heat flow resulting in a greater concentration of data, with another potential driving factor being interest in areas with geothermal energy application (Davies, 2013).

Data

Seismic data

This study uses a combination of 2D and 3D multichannel, post-stack, time-migrated seismic reflection data from offshore Namibia, covering both the shallow- and deep-water sectors of the Lüderitz basin (Fig. 1). The seismic database is correlated with a single exploration well located on the continental shelf, in addition to ODP Site 1084 in the deep-water area.

The 2D seismic data were provided by Spectrum ASA and consists of two surveys conducted in 2006 and 2012 respectively, with further reprocessing in 2012 (to improve image quality in legacy data and to tie 2006 vintage seismic to newly shot 2012 seismic data), and a combined total line length of 752 km (~ 467 mi). The lines have a 4 ms two-way travel time (TWT) sample rate. The frequency range is 3 - 206 Hz (dominant frequency ~ 90 Hz) with a common mid-point (CMP) spacing of 12.5 m (~41 ft) and a shot interval of 25 m (~82 ft). 2006 vintage 2D seismic data was collected with a streamer length of 8100 m (~26575 ft) while 2012 vintage 2D seismic data was collected with a streamer length of 10500 m (~34449 ft).

The 3D seismic survey covers an area of 4150 km^2 (~1602 mi^2) and was acquired for Serica and partners by Polarcus in 2012 using *M/V Polarcus Nadia*. Primary objective of the survey was to establish prospectivity by mapping pinch out structures and a large channel feature in the study area. Streamer length was 8100 m (~26575 ft) with 50 m (~164 ft) source separation of dual source (0.0695 m^3 [2.45 ft^3]) air guns. It is 80-fold with a 4 ms TWT sample rate and Inline spacing of 12.5 m (~41 ft) and Xline spacing of 25 m (~82 ft). 3D pre-stack time migration was conducted by ION GXT. The isotropic frequency range for Kirchhoff pre-stack time migration (PreSTM) ranged between 3-110 Hz. All data were processed through stack and time migration. Velocity model building was done using two iterations of dense residual move out (RMO) auto-picking to create a smooth velocity model constrained by the geological horizons. Velocity model parameters include a 4 ms sample interval, 9000 ms trace length and a 6000 m (~19685 ft) aperture. By parameterising the final velocity model (Fig. 3) for steep dips and high frequency gathers, the amplitude preserving PreSTM resulted in high resolution image gathers and a very high quality final PreSTM seismic image and a high quality, if smooth, velocity model

Figure 3

Well data

Well data included ODP Site 1084 and Norsk Hydro Exploration well 2513/8-1 (Fig. 1). The ODP borehole was drilled as part of ODP Leg 175 with the primary intention of documenting the migration of the Benguela Current along the South Atlantic West African Margin (Wefer et al., 1998). It is located in a water depth of 1992 m (~6535 ft) and targeted the downslope rim of the Lüderitz depositional basin.

The exploration well 2513/8-1 is situated on the shelf in a water depth of 243 m (~797 ft) and targeted a Lower Cretaceous lobe in a thrust ramp graben before terminating in Barremian-Aptian age volcanic rocks at a total depth of 2553 m (~8376 ft). Some sparse BHT data points from this well provide the only available calibration for the temperature estimation workflow.

Method

Figure 4

The temperature estimation workflow utilised in this study is outlined in Fig. 4 and described below. The entirety of the workflow has been developed and tested using commercial software developed for the petroleum industry (Schlumberger Petrel).

The gas hydrate stability field can be utilised to estimate the temperature at the base of the zone of stable gas hydrates, demarcated on seismic by a BSR (Dickens and Quinby-Hunt, 1994; Sloan et al., 1998; Lu and Sultan, 2008). This in turn allows a shallow geothermal gradient across the GHSZ to be estimated and surface heat flow to be estimated (Minshull, 2011; Priyanto, 2018). The stability conditions are controlled in part by the geochemical properties of the fluids available to form clathrate hydrates, which in frontier settings with limited ground truthing are generally assumed to be average salinity (33.5 ‰) seawater and pure

methane (Sloan et al., 1998). Pore fluid pressure conditions are generally assumed to be hydrostatic, equivalent to 0.0101 MPa m^{-1} (~0.446 psi ft^{-1}). The following relationship (Eq. 1) as defined by (Dickens and Quinby-Hunt, 1994) describes methane hydrate stability:

Equation 1: $$\frac{1}{T_{BSR}} = 3.79 \times 10^{-3} - 2.83 \times 10^{-4}(\log P)$$

where T_{BSR} is temperature at the base of GHSZ (K); and P is the corresponding pressure (MPa). Assuming hydrostatic pressure at the BSR depth, temperature at the base of the hydrate stability zone has been established:

Equation 2: $$\mathrm{T}_{BSR} = ((3.79 \times 10^{-3} - 2.83 \times 10^{-4}(\log(\rho \times g \times Z_{BSR})))^{-1}) - 273$$

Where T_{BSR} is the temperature at GHSZ (°C); ρ is density (kg m^{-3}) (of seawater); g is acceleration due to gravity (m s^{-2}) and Z_{BSR} is the depth (m) of the BSR. It must be noted that this is a minimum temperature estimate based on assumed stability field conditions (Dickens, 2001).

The National Oceanic and Atmospheric Administration (NOAA) World Ocean Atlas (WOA) (Boyer et al., 2005) is an open source dataset containing data covering the world's oceans for temperature, salinity, density, etc. Seabed temperature (Eq. 3) was modelled in the study area using a synthetic hydrothermal gradient derived from the closest WOA data nodes, with the misfit from this approach amounting to ±0.4 °C (±0.72 °F) across the water column.

Equation 3:
$$T_{SEABED} = (-1.919 \ln Z + 21.899) \quad \text{if } Z \leq 200$$
$$T_{SEABED} = 525.65 Z^{-0.714} \quad \text{if } 200 < Z < 1000$$
$$T_{SEABED} = -0.0007Z + 4.4905 \quad \text{if } Z \geq 1000$$

where T_{SEABED} is the modelled hydrothermal gradient temperature (°C) and Z is seabed depth (m).

Given both T_{SEABED}, Z_{SEABED} and T_{BSR}, Z_{BSR} at any geographical locality, then the geothermal gradient (dT/dZ) across the GHSZ at that locality is given by the following relationship.

Equation 4: $$\frac{dT}{dZ} GHSZ = \frac{T_{BSR} - T_{SEABED}}{Z_{BSR} - Z_{SEABED}}$$

Where dT/dZ is geothermal gradient (°C km^{-1}); T_{BSR} is temperature at BSR (°C); T_{SEABED} is seabed temperature (°C); Z_{BSR} is depth of BSR (km); Z_{SEABED} is seafloor depth (km).

Alongside thermal gradient, two key thermal properties are the heat flow and thermal conductivity.

Equation 5: $$Q = k \times \frac{dT}{dZ}$$

Where Q is heat flow (mWm^{-2}); k is thermal conductivity (W m^{-1} K^{-1}) (see Section 3.1) and dT/dZ is geothermal gradient (°C km^{-1}).

Fourier's Law of heat conduction (Eq. 5) is crucial to understanding the interplay between heat flow, thermal conductivity, and geothermal gradient. Establishing a shallow linear geothermal gradient using BSRs is well established (Calvès et al., 2010; Serié et al., 2017) and studies have extrapolated this shallow geotherm for traditional basin modelling workflows. This however does not consider the thermal conductivity structure of the subsurface and how it might be possible to utilise seismic reflection velocity data to do so.

Thermal conductivity estimation

Thermal conductivity is a measure of how well heat is conducted through a material (Gu et al., 2017). Difficulty associated with measuring thermal conductivity in boreholes arise from poor contact between the measuring tool and the borehole wall (Horai, 1982). Thus, considerable attention has been devoted to determining methods for estimating thermal conductivity through more easily acquired secondary data such as seismic velocity

277 measurements. Experimental studies have shown that primary controls on thermal
278 conductivity include mineral composition, porosity and fractures (Gegenhuber and Schoen,
279 2012). Seismic wave velocity is also largely controlled by the same factors. Early work by
280 (Horai, 1982) sought to correlate thermal conductivity with other physical properties such as
281 water content, bulk density, porosity and compressional sound wave velocity. The direct
282 approach involves deriving thermal conductivity from physical properties via empirical
283 relationships (Zamora et al., 1993). Estimates of thermal conductivity computed directly from
284 conventional wireline data can be accurate within 0.2 – 0.3 W m^{-1} K^{-1} (~0.116 – 0.173 BTU h^{-1}
285 ft^{-1} $°F^{-1}$) when derived using empirical relationships from sonic velocity data (Hartmann et al.,
286 2005). Such a direct approach has been utilised in this work using experimental data from
287 existing correlation studies (Brigaud et al., 1990; Brigaud & Vasseur, 1989; Esteban et al.,
288 2015; Griffiths et al., 1992; Gunn et al., 2005; Kukkonen & Peltoniemi, 1998; Francis Lucazeau
289 et al., 2004; Mielke et al., 2017; Popov et al., 2003; Popov et al., 1999). This direct empirical
290 approach derived from experimental data has also been tested by the authors in other basins
291 (Sarkar, 2020; Sarkar and Huuse, 2022).
292 Experimental data can vary in terms of the conditions under which it was collected. Most
293 measurements have been taken at ambient pressure and temperature conditions. Binary
294 parameterisation of the experimental datasets allows characterisation of data points
295 collected under similar parameters. Most studies measured thermal conductivity using the
296 optical scanning method (Popov et al., 1999). There are fewer instances in the source datasets
297 of the use of the divided bar method of measuring thermal conductivity (Hyndman and
298 Jolivet, 1976; Evans, 1977). Only wet samples from these studies were used as our case study
299 is in deep water and thus fully saturated with water, gas and/or gas hydrate. In dry samples,
300 the contribution to thermal conductivity arising from lithological heterogeneities (matrix

properties) can be masked by the stronger influence of porosity (Hartmann et al., 2005). In contrast wet samples reflect the impact of porosity and lithological variations.

The range of samples included in our fit cover a wide range of lithologies, including sandstones, limestones, granites, basalts, marble to name a few (Grevemeyer and Villinger, 2001; Hartmann et al., 2005; Boulanouar et al., 2013; Esteban et al., 2015; Jorand et al., 2015; Gu et al., 2017; Mielke et al., 2017). In so doing it is hoped that the resulting empirical relationship will best apply to the broadest possible range of rock types that can be expected subsurface across the study area. It must be noted though that variables within the sample set (Fig. 5) include and are not limited to the porosity (arising from cracks for example). Fractures are known to reduce both P wave velocities and thermal conductivity (Zamora et al., 1993).

A regression through the filtered experimental data points taken from the aforementioned studies gives the following empirical relationship for thermal conductivity:

Equation 6: $$k_V = (0.001 \times V_P) - 0.5071$$

Where k_V is thermal conductivity from velocity (W m^{-1} K^{-1}) and V_P is P wave velocity (m s^{-1}).

Figure 5

Certain trends are evident in the cross plot of sample data in Fig. 5. Due to the lack of salt encountered in the study area, there is a lack of sample points in the expected high conductivities associated with salt (Esteban et al., 2015). The regression is anchored by the large cluster of points associated with the Grevemeyer & Villinger (2001) data. The Hartmann et al. (2005) and Gu et al. (2017) samples are parallel to the best fit regression.

Seismic P wave velocity within the area is converted to thermal conductivity (k_V) using the thermal conductivity relationship (Eq. 6), with velocity averaged down to the depth of the

BSR, Z_{BSR}. The variation in thermal conductivity with depth can be overlain on a 3D seismic reflection dataset in this manner. Using Z_{BSR}, determined on reflection seismic data, the hydrate stability field can be utilised to compute the temperature at this phase boundary for the base of the GHSZ (using Eq. 2). Temperature at the seabed is known from the hydrothermal gradient (given by Eq. 3). A shallow geothermal gradient may thus be computed between seabed and BSR (Eq. 4). As thermal conductivity has been derived from acoustic velocity data, and with shallow geothermal gradient also available, it becomes possible to reapply Fourier's Law (Eq. 5) to derive heat flow for this area through inverse modelling. Estimating the shallow geotherm and heat flow along the full extent of a BSR helps eliminate the bias in heat flow distribution from direct measurements taken at discrete locations (Shankar and Riedel, 2013). This BSR derived heat flow proxy is used in conjunction with the bulk thermal conductivity volume to generate a volume of average geothermal gradient for the bulk volume (rearranging Eq. 5).

Temperature below the seafloor can be summarised as being a function of the depth below the seafloor and the average geothermal gradient. It follows that an estimate of temperature may be arrived at through this simple relationship where the temperature at any given depth point is given by multiplying the average geothermal gradient against the depth to that point:

Equation 7: $$T = T_{SEABED} + (\frac{dT}{dZ} \times Z_{SUBSURFACE})$$

where *T* is predicted temperature (°C); T_{SEABED} is the temperature at seabed (°C); *dT/dZ* is the average geothermal gradient (°C km^{-1}); and $Z_{SUBSURFACE}$ is the subsurface depth (km). Seabed temperature is added to account for the effect of the hydrothermal gradient on the subsurface temperatures.

As the average geothermal gradient is only valid for the subsurface and due to the seismic input volume containing the water column it becomes necessary to negate the latter. Without flattening the volume to the seabed, it is instead possible to use the seabed depth map to derive a depth volume relative to seabed depth.

Equation 8: $$Z_{SUBSURFACE} = Z - Z_{SEABED}$$

where $Z_{SUBSURFACE}$ is the subsurface depth (km); Z is the absolute depth (km); and Z_{SEABED} is the seabed depth (km).

The steps outlined above are all possible using basic functions available within the Petrel seismic interpretation suite. A pillar grid corresponding to the extent of the seismic survey is built with voxel sizes of 50 m * 50 m * 10 m (~164 ft * 164 ft * 32.8 ft). The original seismic reflection and velocity data can be resampled into the pillar grid. It must be noted that resampling the original data may result in a loss of fidelity from the algorithm used and the size of the voxels comprising the model. The advantage of using such a pillar grid is that computation of the various properties such as velocity derived thermal conductivity (k_V) become easier. It is also easier to model pseudo-wells in this manner.

Uncertainty modelling

An attempt to model uncertainty was made following the use of 95% confidence interval method as used by Phrampus et al. (2017) to derive bounds for both the heat flow proxy from BSR and the overall temperature prediction. The approach to calculating these bounds can be considered modular for the two aforementioned predicted thermal properties, with the same workflow (Fig. 4) also used here but with an upper bound and lower bound approach for each step as shown in Table 1. For example, to model the lower bound of the shallow heat flow proxy, firstly the lower bound of the root mean square (RMS) of interval velocity across the

GHSZ is used to domain convert the TWT BSR pick. This has the effect of varying the BSR in depth, to a shallower depth because of the lower interval velocity selected which in turn would result in a lower temperature for the BSR using the phase relationship described previously. It must be noted that the hydrate phase composition is not varied and that the pressure field is unaltered from previous modelling. Similarly, the seabed depth and temperature are considered unchanged. This gives the lower bound for geothermal gradient. Using the 1D approximation of Fourier's law (Eq. 5) this lower bound geothermal gradient is convolved with the lower bound regression for thermal conductivity from velocity separate from that discussed in Section 3.1 but based on the same 95% confidence interval. This results in the lower bound of the heat flow estimate from the BSR. Using the opposite bound of the various component steps helps arrive at the upper bound for heat flow. The bounds for the temperature prediction can be simplified to varying the bulk thermal conductivity volume and conditioning the model with the upper and lower bound heat flow from BSR. This gives an envelope of temperatures representing the spread of values possible using 95% confidence for all input parameters.

Table 1

Results

The BSR observed in the area has been mapped across the NW and SW quadrants of the 3D reflection seismic coverage (Fig. 6). Though the full extent of the visible BSR was mapped, only the extent corresponding to the highest confidence seismic picks are displayed as the clarity of the BSR degrades towards the edges. This should preclude any resulting anomalous artefacts and edge effects. It is this high confidence extent of the BSR that is referred to in the following sections unless otherwise specified. The BSRs are found to have opposite seismic reflection polarity to the seabed reflection indicating the likelihood of gas hydrate above free gas (Kretschmer et al., 2015). Though there is no record of hydrates from ODP Site 1084, high amplitude reflections are observed to occur in close proximity below the BSR (Fig. 2a), characteristic of the presence of trapped gas. Temperature at BSR depth and the phase relationship used to determine this is shown in Fig. 6.

Figure 6

Neither the exploration well nor ODP Site 1084 fall within the bounds of the thermal model. As a result, direct calibration is not possible. However well 2513/8-1 contains BHT information that may provide some calibration for the predicted results. Pseudo-wells provide a means of simulating 2513/8-1 at a comparable location along strike (Fig. 1a). Pseudo-well P1 is projected into the study area following bathymetric contours as close as possible along strike from 2513/8-1, to maintain structural parity. BHT recordings typically are lower than actual formation temperature due to cooling effect of circulating fluids in a borehole and thus they must be corrected (Deming, 1989). There are insufficient points for a Horner correction (Horner, 1951; Bonté et al., 2012) to be applied and hence a rudimentary correction is made

for time since circulation (see https://www.zetaware.com/utilities/bht/timesince.html first accessed August 2018). The predicted temperatures are between 17 and 26% higher than the corrected BHT (Fig. 7a).

Figure 7

On seismic data it was evident that there is a deeply incised canyon like structure trending NE – SW that can be seen in the north-eastern most extent of the seismic volume (Wanke and Toirac-proenza, 2018). This corresponds to the location of P1, which is seen to intersect the channel fill structures of this canyon. It becomes evident then that though P1 was projected into the seismic volume maintaining bathymetric parity, in the subsurface, due to the occurrence of this channel like geometry, it is not possible to maintain stratigraphic parity to 2513/8-1. This is surmised to be the primary factor for the misfit with BHT seen.

Further pseudo-wells (T1 – 3) were modelled to examine the change in thermal profile moving from the proximal section to the distal part of the study area. The results (Fig. 7) display what the thermal profile in these pseudo-wells would be like if a typical geothermal gradient of 30 °C km^{-1} or 40 °C km^{-1} (87 °F mi^{-1} or 116 °F mi^{-1}, respectively) was applied linearly from seabed. The temperature window considered prospective for reservoirs at the present day has been referred to as the Golden Zone (60 – 120 °C [140 – 248 °F]) (Nadeau, 2011). It becomes apparent then that the varying geothermal gradient with depth of the proposed model would significantly alter the subsurface depth at which the Golden Zone would begin and end in comparison to the typical linear geothermal gradients that are often considered in a traditional basin modelling workflow. Analysing the geothermal gradient between these pseudo-wells it is seen that in the proximal section (T1) there is a much steeper drop off (~57.1 °C km^{-1} [165 °F mi^{-1}] in the uppermost 800 m [~2625 ft] to 15 °C km^{-1} [43 °F mi^{-1}] in the deepest 1000 m [~3281 ft]) compared to the intermediate (T2) and deeper sections (T3). The spread

of isotherms in a dip section (Fig. 8) reflects this. Isotherm spacing is regular in the Mesozoic section moving into deeper water. However, in the proximal end corresponding to minimal Tertiary cover, there is observed the greatest divergence between isotherms in Mesozoic sediment. Temperature for the Aptian 'Kudu shale' source rock in the region has also been mapped (Fig. 8).

Figure 8

Below both BSRs, but particularly the northern BSR (Fig. 6), the effects of gas blanking were observed in the seismic reflection data. An average interval velocity extraction reveals anomalously low values within this area (Fig. 8). Pseudo-well T4 was modelled to capture this area. These results are consistent with the deep-water pseudo-well T3 with similar geothermal gradient at each 1000 m (~3281 ft) interval between the two pseudo-wells.

Discussion

Uncertainty

In a quantitative workflow such as the one discussed in the paper, there are multiple avenues for uncertainty in the constituent steps. Previous literature includes attempts to quantify the cumulative uncertainty in predictions using a BSR derived geothermal gradient (5 – 35%) and heat flow (10 – 50%) (Grevemeyer and Villinger, 2001). Such attempts have usually quantified uncertainty for the component steps rather than the compound uncertainty for the entire process. The parameter-based error in BSR heat flow could lead to a disparity of up to 25% with measured heat flow (He et al., 2009). For this work, with a lack of well data for ground truthing, the temperature estimation bounds for 95% confidence were used to give an idea of the range within which the estimates can vary. It is important to note the impact of variability in input factors for the component steps. For example, results from the Blake Ridge show that actual temperatures at the BSR depth could be between 0.5 – 2.9 °C (0.9 – 5.2 °F) lower than the temperature predicted by the hydrate phase relationship for that particular depth and pressure (Wood and Ruppel, 2000). This implies that a significant source of uncertainty in the thermal modelling could result from the assumptions made about the conditions at the base of the GHSZ. As stated earlier, an assumption has been made on the lattice fluid and trapped gas mix for the hydrate zone in the absence of direct piston core

sampling. Varying gas compositions can vary the hydrate stability and thus alter the temperature at the bottom simulating reflector (Chand et al., 2008). The prevalence of methane hydrates globally leads us to assume it is the most likely composition of the hydrates in the study area.

As the temperature dependency of gas hydrate is a key component of RST applied without direct temperature measurements, factors causing hydrate instability can also introduce uncertainty. Instability can be caused by various factors such as relatively recent warming or varying sea level, isostatic rebound, and tectonic uplift affecting the ambient pressure at the BSR (Li et al., 2017; Burton et al., 2020).

BWT fluctuations, both the magnitude and time scale for which they occur provide another element of uncertainty. It must be noted that the strong Benguela Current flows along the Namibian margin in this area (Putuhena et al., 2021)and it is difficult to directly factor in the impact that ocean current fluctuations may have on the modelling. The data used to generate a model of the hydrothermal gradient in the area utilised NOAA data that have been averaged annually over an eight-year period, but glacial-interglacial BWT changes are poorly known and thus difficult to factor in. Hence, in the absence of evidence to the contrary we assume the BSRs observed are in thermal equilibrium and recognise this carries an inherent uncertainty.

The quality of the initial velocity model is another source of uncertainty. As thermal conductivity is derived from it using a direct empirical relationship, any anomalies in the existing velocity model or velocity data will be translated into the derived properties. From the low spread of RMS interval velocities for the GHSZ it is apparent the application of a default 1500 m s^{-1} (~4921 ft s^{-1}) velocity above seabed during the velocity model building stage results in a heavily smoothed velocity model. This is expected to be reflected in the nature of the temperature profile generated using velocities as input.

In this study, BSRs are used to derive the geotherm of the shallow subsurface hydrate stability field and heat flow. One of the uncertainties to this approach is the thermal conductivity of the rock column below the BSR (Burton et al., 2020). Burton et al. (2020) have shown that in a case of variable basal heat flow, BSR depth may be constant due to varying sub-BSR thermal conductivity (conversely if basal heat flow is constant, BSR depth may vary due to differences in sub-BSR thermal conductivity). In the RST approach, variability in sub-BSR thermal conductivity is accounted for in the bulk transformation of velocities to thermal conductivity. In the Blake Ridge example (Sarkar, 2020), borehole velocities available below the GHSZ were used to convert to thermal conductivity, and then used to approximate a surface heat flow proxy. If heat flow results calibrate from this approach, it would suggest that this effect has been mitigated.

In the absence of a reliable heat flow recording for this area, a BSR derived heat flow proxy has been used. This is a shallow heat flow as it uses an average velocity derived thermal conductivity and geothermal gradient valid within the GHSZ (Eq. 5). Unlike in traditional basin modelling the radiogenic heat production of the rock column has not been integrated. Instead, this solitary heat flow proxy has been used to condition the model for an average geothermal gradient. Though hydrothermal fluid circulation in the subsurface can also greatly alter heat flow, both vertically and laterally, the study area is likely to be minimally impacted in this regard. As the study area is sufficiently distant from a neighbouring seamount to negate the convective and advective heat flow impact of hydrothermal fluid circulation, heat transport in this area is predominantly conductive. Therefore, the assumption is of limited lateral heat flow variability, which is backed by the BSR-derived thermal gradients and derivative heat flow estimates. In a separate case study covering the data rich North Sea, it has been shown that RST can be conducted successfully using laterally varying shallow heat

509 flow as a parameter input (Sarkar, 2020). An estimate of the uncertainty of the heat flow
510 derived in this manner has been computed using the method shown in Phrampus et al. (2017).
511 Heat flow is found to range between 46.2 – 76.2 mWm^{-2} (~0.01465 – 0.02416 BTU h^{-1} ft^{-2}),
512 with the weighted mean for the heat flow used for computation of the temperature model
513 equal to 64 mWm^{-2} (~0.02022 BTU h^{-1} ft^{-2}). The lower bound of the derived ranged is
514 consistent with results from Macgregor (2020) while the upper bound would be in line with
515 the preferred prediction from the global map in Lucazeau (2019). The weighted mean is
516 interestingly consistent with the continental margin heat flow mean reported by Davies
517 (2013). The heat flow range given by the bounds is consistent with observational data and
518 estimations of heat flow from age relationships corresponding to this area (Hamza and Vieira,
519 2012).

520 The BSR expression itself may be another source of uncertainty. The BSR based thermal
521 modelling is predicated on the understanding that its expression is along the base of the
522 GHSZ. In some instances though, multiple stacked BSRs might be observed (Popescu et al.,
523 2006), with gas hydrate occurring below it (Paganoni et al., 2016). These have been
524 speculated to be paleo/relict BSRs (Hornbach et al., 2003) or a consequence of there being a
525 mixed phase boundary (Paganoni et al., 2016). For this work, the BSR is assumed to be
526 representative of the phase boundary for methane hydrate stability.

527 ## *Implications*

528 As stated previously, the source maturity of the Aptian Kudu Shale interval in the Lüderitz
529 Basin is a key unknown in terms of the petroleum systems elements. With the thermal
530 modelling workflow indicating an average temperature of 134 °C (272.3 °F) across the top of
531 the Barremian Prospect B structure (Fig. 8a), the base of the overlying Kudu shale source rock

532 immediately above would therefore lie in the gas generation window (Bjørlykke et al., 1989).
533 This is consistent with the nearby Kudu fields which produce gas condensate from the same
534 Aptian source interval (Van Der Spuy, 2003; Schmidt, 2004; Samakinde et al., 2021). The
535 results thus suggest that the Lüderitz Basin has the potential for a working hydrocarbon
536 system with gas charged reservoirs.

537 This study estimated present day temperature at key subsurface target depths in a frontier
538 setting in the absence of any substantive well control. The workflow presented enables
539 seismic operators to utilise data libraries of seismic reflection and velocity data to generate
540 present day estimations of subsurface temperature in a non-invasive manner, prior to an
541 expensive drilling campaign. It is hoped that this will help streamline petroleum systems
542 analysis and provide an additional dataset for basin modellers to use help minimise
543 exploration uncertainty.

544 Conclusions

545 The RST model proposed in this study is a simple and robust methodology for estimation of
546 present-day subsurface temperature in frontier areas lacking borehole control for
547 temperatures (such as the Lüderitz Basin). It makes use of readily available seismic reflection
548 and velocity data in a workflow developed on an industry standard software suite. It highlights
549 how established workflows for BSR derived heat flow may be combined with existing
550 experimental thermal conductivity and velocity data for various lithologies to develop an
551 empirical transform that may be used to generate a thermal conductivity volume from seismic
552 velocity models. Given thermal conductivity and P wave velocity have sensitivity to similar
553 parameters, this methodology allows the user to examine the vertical and lateral variability
554 in thermal properties in a frontier basin especially when high-quality pre-SDM and FWI

555 velocity models are available. Indications from RST suggest that the key Aptian source interval
556 along this margin (the Kudu Shale) is in the gas generative window, based on an average
557 predicted basal temperature 134 °C. The immediately underlying primary Barremian Prospect
558 B structure is therefore deeper than the threshold temperature for the Golden Zone in
559 reservoirs. The gas hydrate based heat flow proxy averages 64 mW m^{-2} in this basin.

560 References

561 Allen, P., and J. Allen, 2013, Basin analysis: principles and application to petroleum play
562 assessment.

563 Bagguley, J., and S. Prosser, 1999, The interpretation of passive margin depositional processes
564 using seismic stratigraphy: examples from offshore Namibia: Geological Society, London,
565 Special Publications, v. 153, no. 1, p. 321–344, doi:10.1144/GSL.SP.1999.153.01.20.

566 Bauer, K., S. Neben, B. Schreckenberger, R. Emmermann, K. Hinz, N. Fechner, K. Gohl, A.
567 Schulze, R. B. Trumbull, and K. Weber, 2000, Deep structure of the Namibia continental
568 margin as derived from integrated geophysical studies: Journal of Geophysical Research:
569 Solid Earth, v. 105, no. B11, p. 25829–25853, doi:10.1029/2000JB900227.

570 Beardsmore, G., and J. Cull, 2001, Crustal Heat Flow: A Guide to Measurement and Modelling:
571 doi:10.1017/S0016756803218021.

572 Becker, J. J. et al., 2009, Global Bathymetry and Elevation Data at 30 Arc Seconds Resolution:
573 SRTM30_PLUS: Marine Geodesy, v. 32, no. 4, p. 355–371,
574 doi:10.1080/01490410903297766.

575 Berger, W., G. Wefer, C. Richter, C. Lange, J. Girardeau, O. Hemelin, and Shipboard Scientific
576 Party, 1998, 17. The Angola-Benguela upwelling system: Paleoceanographic synthesis of
577 shipboard results from Leg 175: Proceedings of the Ocean Drilling Program, v. 175, p.
578 505–531.

579 Bjørlykke, K., M. Ramm, and G. C. Saigal, 1989, Sandstone diagenesis and porosity
580 modification during basin evolution: Geologische Rundschau, v. 78, no. 1, p. 243–268,
581 doi:10.1007/BF01988363.

582 Bonté, D., J. D. Van Wees, and J. M. Verweij, 2012, Subsurface temperature of the onshore
583 Netherlands: New temperature dataset and modelling: Geologie en
584 Mijnbouw/Netherlands Journal of Geosciences, v. 91, no. 4, p. 491–515,
585 doi:10.1017/S0016774600000354.

586 Boulanouar, A., A. Rahmouni, M. Boukalouch, A. Samaouali, Y. Géraud, M. Harnafi, and J.
587 Sebbani, 2013, Determination of Thermal Conductivity and Porosity of Building Stone
588 from Ultrasonic Velocity Measurements: Geomaterials, v. 03, no. 04, p. 138–144,
589 doi:10.4236/gm.2013.34018.

590 Boyer, T., S. Levitus, H. Garcia, R. A. Locarnini, C. Stephens, and J. Antonov, 2005, Objective
591 analyses of annual, seasonal, and monthly temperature and salinity for the World Ocean
592 on a 0.25° grid: International Journal of Climatology, v. 25, no. 7, p. 931–945,
593 doi:10.1002/joc.1173.

Bray, R., S. Lawrence, and R. Swart, 1998, Namibia License Blocks , Wells: Oil and Gas Journal, v. 96, no. 32, p. 84–88.

Brigaud, F., D. S. Chapman, and S. Le Douaran, 1990, Estimating thermal conductivity in sedimentary basins using lithologic data and geophysical well logs: American Association of Petroleum Geologists Bulletin, v. 74, no. 9, p. 1459–1477, doi:10.1306/0C9B2501-1710-11D7-8645000102C1865D.

Brigaud, F., and G. Vasseur, 1989, Mineralogy, porosity and fluid control on thermal conductivity of sedimentary rocks: Geophysical Journal International, v. 98, no. 3, p. 525–542, doi:10.1111/j.1365-246X.1989.tb02287.x.

Bullard, E. C., 1939, Heat flow in South Africa: Proceedings of the Royal Society of London. Series A. Mathematical and Physical Sciences, v. 173, no. 955, p. 474–502, doi:10.1098/rspa.1939.0159.

Burton, Z. F. M., J. P. Cassanelli, T. Mukerji, and S. A. Graham, 2020, Impact of Sub-Gas Hydrate Sediment Thermal Conductivity on Hydrate-Based Heat Flow Derivations, *in* AGU Fall Meeting Abstracts: American Geophysical Union, p. OS029-0009.

Burton, Z. F. M., K. F. Kroeger, A. Hosford Scheirer, Y. Seol, B. Burgreen-Chan, and S. A. Graham, 2020, Tectonic Uplift Destabilizes Subsea Gas Hydrate: A Model Example From Hikurangi Margin, New Zealand: Geophysical Research Letters, v. 47, no. 7, doi:10.1029/2020GL087150.

Burton, Z. F. M., J. M. Moldowan, L. B. Magoon, R. Sykes, and S. A. Graham, 2019, Interpretation of source rock depositional environment and age from seep oil, east coast of New Zealand: International Journal of Earth Sciences, v. 108, no. 4, p. 1079–1091, doi:10.1007/s00531-018-01675-6.

Burton, Z. F. M., J. M. Moldowan, R. Sykes, and S. A. Graham, 2018, Unraveling Petroleum Degradation, Maturity, and Mixing and Addressing Impact on Petroleum Prospectivity: Insights from Frontier Exploration Regions in New Zealand: Energy & Fuels, v. 32, no. 2, p. 1287–1296, doi:10.1021/acs.energyfuels.7b03261.

Calvès, G., M. Huuse, A. Schwab, and P. Clift, 2008, Three-dimensional seismic analysis of high-amplitude anomalies in the shallow subsurface of the Northern Indus Fan: Sedimentary and/or fluid origin: Journal of Geophysical Research, v. 113, no. B11, p. B11103, doi:10.1029/2008JB005666.

Calvès, G., A. M. Schwab, M. Huuse, P. D. Clift, and A. Inam, 2010, Thermal regime of the northwest Indian rifted margin - Comparison with predictions: Marine and Petroleum Geology, v. 27, no. 5, p. 1133–1147, doi:10.1016/j.marpetgeo.2010.02.010.

Chand, S., J. Mienert, K. Andreassen, J. Knies, L. Plassen, and B. Fotland, 2008, Gas hydrate stability zone modelling in areas of salt tectonics and pockmarks of the Barents Sea suggests an active hydrocarbon venting system: Marine and Petroleum Geology, v. 25, no. 7, p. 625–636, doi:10.1016/j.marpetgeo.2007.10.006.

Crameri, F., G. E. Shephard, and P. J. Heron, 2020, The misuse of colour in science communication: Nature Communications, v. 11, no. 1, p. 5444, doi:10.1038/s41467-020-19160-7.

Davies, J. H., 2013, Global map of solid Earth surface heat flow: Geochemistry, Geophysics, Geosystems, v. 14, no. 10, p. 4608–4622, doi:10.1002/ggge.20271.

Davies, J. H., and D. R. Davies, 2010, Earth's surface heat flux: Solid Earth, v. 1, no. 1, p. 5–24, doi:10.5194/se-1-5-2010.

639 Davis, E. E., K. Wang, K. Becker, R. E. Thomson, and I. Yashayaev, 2003, Deep-ocean
640 temperature variations and implications for errors in seafloor heat flow determinations:
641 Journal of Geophysical Research: Solid Earth, v. 108, no. B1, p. 1–6,
642 doi:10.1029/2001JB001695.
643 Davison, I., L. Anderson, and P. Nuttall, 2012, Salt deposition, loading and gravity drainage in
644 the Campos and Santos salt basins: Geological Society, London, Special Publications, v.
645 363, no. 1, p. 159–174, doi:10.1144/SP363.8.
646 Deming, D., 1989, Application of bottom-hole temperature corrections in geothermal studies:
647 Geothermics, v. 18, no. 5–6, p. 775–786, doi:10.1016/0375-6505(89)90106-5.
648 Dickens, G. R., 2001, Modeling the Global Carbon Cycle with a Gas Hydrate Capacitor:
649 Significance for the Latest Paleocene Thermal Maximum, *in* C. K. Paull, and W. P. Dillon,
650 eds., Natural gas hydrates: occurrence, distribution, and detection: Washington, D. C.,
651 AGU, p. 19–38, doi:10.1029/GM124p0019.
652 Dickens, G. R., and M. S. Quinby-Hunt, 1994, Methane hydrate stability in seawater:
653 Geophysical Research Letters, v. 21, no. 19, p. 2115–2118, doi:10.1029/94GL01858.
654 Esteban, L., L. Pimienta, J. Sarout, C. D. Piane, S. Haffen, Y. Geraud, and N. E. Timms, 2015,
655 Study cases of thermal conductivity prediction from P-wave velocity and porosity:
656 Geothermics, v. 53, p. 255–269, doi:10.1016/j.geothermics.2014.06.003.
657 Evans, T. R., 1977, Thermal Properties of North Sea Rocks.: Log Analyst, v. 18, no. 2, p. 3–12.
658 Frost, B. R., and P. N. Shive, 1986, Magnetic mineralogy of the lower continental crust: Journal
659 of Geophysical Research, v. 91, no. B6, p. 6513, doi:10.1029/JB091iB06p06513.
660 Fuchs, S., and N. Balling, 2016, Improving the temperature predictions of subsurface thermal
661 models by using high-quality input data. Part 2: A case study from the Danish-German
662 border region: Geothermics, v. 64, p. 1–14, doi:10.1016/j.geothermics.2016.04.004.
663 Gegenhuber, N., and J. Schoen, 2012, New approaches for the relationship between
664 compressional wave velocity and thermal conductivity: Journal of Applied Geophysics, v.
665 76, p. 50–55, doi:10.1016/j.jappgeo.2011.10.005.
666 Gladczenko, T. P., J. Skogseid, and O. Eldhom, 1998, Namibia volcanic margin: Marine
667 Geophysical Researches, v. 20, no. 4, p. 313–341, doi:10.1023/A:1004746101320.
668 Gosnold, W., and B. Panda, 2002, The Global Heat Flow Database of the International Heat
669 Flow Commission: doi:http://doi.org/10.17616/R3G305.
670 Goutorbe, B., J. Poort, F. Lucazeau, and S. Raillard, 2011, Global heat flow trends resolved
671 from multiple geological and geophysical proxies: Geophysical Journal International, v.
672 187, no. 3, p. 1405–1419, doi:10.1111/j.1365-246X.2011.05228.x.
673 Grevemeyer, I., and H. Villinger, 2001, Gas hydrate stability and the assessment of heat flow
674 through continental margins: Geophysical Journal International, v. 145, p. 647–660,
675 doi:ISI:000169428800007.
676 Griffiths, C. M., N. R. Brereton, R. Beausillon, and D. Castillo, 1992, Thermal conductivity
677 prediction from petrophysical data: a case study: Geological Applications of Wireline
678 Logs II, v. 65, no. 1, p. 299–315, doi:10.1144/GSL.SP.1992.065.01.23.
679 Gu, Y., W. Rühaak, K. Bär, and I. Sass, 2017, Using seismic data to estimate the spatial
680 distribution of rock thermal conductivity at reservoir scale: Geothermics, v. 66, p. 61–72,
681 doi:10.1016/j.geothermics.2016.11.007.
682 Gunn, D. A., L. D. Jones, M. G. Raines, D. C. Entwisle, and P. R. N. Hobbs, 2005, Laboratory
683 measurement and correction of thermal properties for application to the rock mass:

684 Geotechnical and Geological Engineering, v. 23, no. 6, p. 773–791, doi:10.1007/s10706-
685 003-3156-6.
686 Haacke, R. R., G. K. Westbrook, and R. D. Hyndman, 2007, Gas hydrate, fluid flow and free gas:
687 Formation of the bottom-simulating reflector: Earth and Planetary Science Letters, v.
688 261, no. 3–4, p. 407–420, doi:10.1016/j.epsl.2007.07.008.
689 Hamza, V. M., and F. P. Vieira, 2012, Global distribution of the lithosphere-asthenosphere
690 boundary: A new look: Solid Earth, v. 3, no. 2, p. 199–212, doi:10.5194/se-3-199-2012.
691 Harper, M. L., 1971, Approximate geothermal gradients in the North Sea basin: Nature, v. 230,
692 no. 5291, p. 235–236, doi:10.1038/230235a0.
693 Hartmann, A. Ã., V. Rath, and C. Clauser, 2005, Thermal conductivity from core and well log
694 data: International Journal of Rock Mechanics and Mining Sciences, v. 42, no. 7- 8 SPEC.
695 ISS., p. 1042–1055, doi:10.1016/j.ijrmms.2005.05.015.
696 Hasterok, D., 2010, Thermal State of Continental and Oceanic Lithosphere: The University of
697 Utah, 168 p.
698 Hasterok, D., D. S. Chapman, and E. E. Davis, 2011, Oceanic heat flow: Implications for global
699 heat loss: Earth and Planetary Science Letters, v. 311, no. 3–4, p. 386–395,
700 doi:10.1016/j.epsl.2011.09.044.
701 He, L., J. Wang, X. Xu, J. Liang, H. Wang, and G. Zhang, 2009, Disparity between measured and
702 BSR heat flow in the Xisha Trough of the South China Sea and its implications for the
703 methane hydrate: Journal of Asian Earth Sciences, v. 34, no. 6, p. 771–780,
704 doi:10.1016/j.jseaes.2008.11.004.
705 Hodgson, N., A. Intawong, K. Rodriguez, and M. Huuse, 2014, A seismic tool to reduce source
706 maturity risk in unexplored basins: First Break, v. 32, no. 3, p. 103–108.
707 Hokstad, K., Z. A. Tašárová, S. A. Clark, R. Kyrkjebø, K. Duffaut, C. Fichler, and T. Wiik, 2017,
708 Radiogenic heat production in the crust from inversion of gravity and magnetic data:
709 Norsk Geologisk Tidsskrift, v. 97, no. 3, p. 241–254, doi:10.17850/njg97-3-04.
710 Horai, K., 1982, Thermal Conductivity of Sediments and Igneous Rocks Recovered during Deep
711 Sea Drilling Project Leg 60, *in* D. M. Hussong, and S. Uyeda, eds., Initial Reports of the
712 Deep Sea Drilling Project, 60: U.S. Government Printing Office, p. 807–834,
713 doi:10.2973/dsdp.proc.60.149.1982.
714 Hornbach, M. J., W. S. Holbrook, A. R. Gorman, K. L. Hackwith, D. Lizarralde, and I. Pecher,
715 2003, Direct seismic detection of methane hydrate on the Blake Ridge: Geophysics, v.
716 68, no. 1, p. 92–100, doi:10.1190/1.1543196.
717 Horner, D. R., 1951, Pressure build-up in wells, *in* 3rd World Petroleum Congress Proceedings:
718 p. WPC-4135.
719 Hunt, J. M., 1984, Generation and Migration of Light Hydrocarbons: Science, v. 226, no. 4680,
720 p. 1265–1270, doi:10.1126/science.226.4680.1265.
721 Hyndman, R. D., and J. Jolivet, 1976, Heat Flow Measurements in Deep Crustal Holes on the
722 Mid-Atlantic Ridge: v. 81, no. 23, p. 4053–4060.
723 Hyndman, R. D., G. D. Spence, R. Chapman, M. Riedel, and R. N. Edwards, 2001, Geophysical
724 Studies of Marine Gas Hydrate in Northern Cascadia, *in* C. K. Paull, and W. P. Dillon, eds.,
725 Natural Gas Hydrates: Occurrence, Distribution, and Detection: Washington, D. C., AGU,
726 p. 273–295, doi:10.1029/GM124p0273.
727 Intawong, A., M. Huuse, K. Rodriguez, N. Hodgson, and M. Negonga, 2015, Further de-risking
728 source rock maturity in the Luderitz Basin using basin modelling to support the BSR-

729 derived near-surface geotherm: First Break, v. 33, no. October, p. 71–76.
730 Jaupart, C., J. C. Mareschal, and L. Iarotsky, 2016, Radiogenic heat production in the
731 continental crust: Lithos, v. 262, p. 398–427, doi:10.1016/j.lithos.2016.07.017.
732 Jorand, R., C. Clauser, G. Marquart, and R. Pechnig, 2015, Statistically reliable petrophysical
733 properties of potential reservoir rocks for geothermal energy use and their relation to
734 lithostratigraphy and rock composition: The NE Rhenish Massif and the Lower Rhine
735 Embayment (Germany): Geothermics, v. 53, p. 413–428,
736 doi:10.1016/j.geothermics.2014.08.008.
737 Karner, G. D., and N. W. Driscoll, 1999, Tectonic and stratigraphic development of the West
738 African and eastern Brazilian Margins: insights from quantitative basin modelling:
739 Geological Society, London, Special Publications, v. 153, no. 1, p. 11–40,
740 doi:10.1144/GSL.SP.1999.153.01.02.
741 Kretschmer, K., A. Biastoch, L. Rüpke, and E. Burwicz, 2015, Modeling the fate of methane
742 hydrates under global warming: Global Biogeochemical Cycles, v. 29, no. 5, p. 610–625,
743 doi:10.1002/2014GB005011.
744 Kukkonen, I. T., and S. Peltoniemi, 1998, Relationships between thermal and other
745 petrophysical properties of rocks in Finland: Physics and Chemistry of the Earth, v. 23,
746 no. 3, p. 341–349, doi:10.1016/S0079-1946(98)00035-4.
747 Kvenvolden, K. A., and T. D. Lorenson, 2001, The Global Occurrence of Natural Gas Hydrate,
748 *in* C. K. Paull, and W. P. Dillon, eds., Natural Gas Hydrates: Occurrence, Distribution, and
749 Detection: Washington, D. C., AGU, p. 3–18, doi:10.1029/GM124p0003.
750 Langel, R. A., and W. J. Hinze, 1998, The magnetic field of the Earth's lithosphere: the satellite
751 perspective: Cambridge University Press, 429 p., doi:10.1029/99eo00111.
752 Le, A. N., M. Huuse, J. Redfern, R. L. Gawthorpe, and D. Irving, 2015, Seismic characterization
753 of a Bottom Simulating Reflection (BSR) and plumbing system of the Cameroon margin,
754 offshore West Africa: Marine and Petroleum Geology, v. 68, p. 629–647,
755 doi:10.1016/j.marpetgeo.2014.12.006.
756 Li, A., R. J. Davies, and S. Mathias, 2017, Methane hydrate recycling offshore of Mauritania
757 probably after the last glacial maximum: Marine and Petroleum Geology, v. 84, p. 323–
758 331, doi:10.1016/j.marpetgeo.2017.04.007.
759 Light, M. P. R., M. P. Maslanyj, R. J. Greenwood, and N. L. Banks, 1993, Seismic sequence
760 stratigraphy and tectonics offshore Namibia: Tectonics and seismic sequence
761 stratigraphy, v. 71, no. 1, p. 163–191, doi:10.1144/GSL.SP.1993.071.01.08.
762 Lister, C. R. B., 1972, On the Thermal Balance of a Mid-Ocean Ridge: Geophysical Journal
763 International, v. 26, no. 5, p. 515–535, doi:10.1111/j.1365-246X.1972.tb05766.x.
764 Locarnini, R. A. et al., 2013, WORLD OCEAN ATLAS 2013: Temperature Volume 1: 52 p.,
765 doi:10.7289/V55X26VD.
766 Lu, Z., and N. Sultan, 2008, Empirical expressions for gas hydrate stability law, its volume
767 fraction and mass-density at temperatures 273.15K to 290.15K: Geochemical Journal, v.
768 42, no. 2, p. 163–175, doi:10.2343/geochemj.42.163.
769 Lucazeau, F., 2019, Analysis and Mapping of an Updated Terrestrial Heat Flow Data Set:
770 Geochemistry, Geophysics, Geosystems, v. 20, no. 8, p. 4001–4024,
771 doi:10.1029/2019GC008389.
772 Lucazeau, F., F. Brigaud, and J. L. Bouroullec, 2004, High-resolution heat flow density in the
773 lower Congo basin: Geochemistry, Geophysics, Geosystems, v. 5, no. 3, p. Q03001,

774 doi:10.1029/2003GC000644.
775 Macgregor, D. S., 2020, Regional variations in geothermal gradient and heat flow across the
776 African plate: Journal of African Earth Sciences, v. 171, p. 103950,
777 doi:10.1016/j.jafrearsci.2020.103950.
778 Magoon, L. B., and W. G. Dow, 1994, The Petroleum System: Chapter 1: Part I. Introduction,
779 *in* The Petroleum System--From Source to Trap: AAPG Memoir, p. 3–24.
780 McCarthy, K., K. Rojas, M. Niemann, D. Palmowski, K. Peters, and A. Stankiewicz, 2011, Basic
781 Petroleum Geochemistry for Source Rock Evaluation: Oilfield Review, v. 23, no. 2, p. 32–
782 43.
783 Mello, M. R., A. A. Bender, N. C. A. Filho, S. Barbanti, M. R. Franke, and C. L. C. Jesus, 2011,
784 Correlation of the Petroleum System from Santos and Namibian Offshore Basins, *in* OTC
785 Brasil: Offshore Technology Conference, p. 1–16, doi:10.4043/22813-MS.
786 Mielke, P., K. Bär, and I. Sass, 2017, Determining the relationship of thermal conductivity and
787 compressional wave velocity of common rock types as a basis for reservoir
788 characterization: Journal of Applied Geophysics, v. 140, p. 135–144,
789 doi:10.1016/j.jappgeo.2017.04.002.
790 Minshull, T. A., 2011, Some comments on the estimation of geothermal gradients from the
791 depths of bottom simulating reflectors, *in* Proceedings of the 7th international
792 conference on gas hydrates: p. 1–8.
793 Nadeau, P. H., 2011, Earth's energy "Golden Zone": a synthesis from mineralogical research:
794 Clay Minerals, v. 46, no. 1, p. 1–24, doi:10.1180/claymin.2011.046.1.1.
795 Paganoni, M., J. A. Cartwright, M. Foschi, R. C. Shipp, and P. Van Rensbergen, 2016, Structure
796 II gas hydrates found below the bottom-simulating reflector: Geophysical Research
797 Letters, v. 43, no. 11, p. 5696–5706, doi:10.1002/2016GL069452.
798 Phrampus, B. J., R. N. Harris, and A. M. Tréhu, 2017, Heat flow bounds over the Cascadia
799 margin derived from bottom simulating reflectors and implications for thermal models
800 of subduction: Geochemistry, Geophysics, Geosystems, v. 18, no. 9, p. 3309–3326,
801 doi:10.1002/2017GC007077.
802 Popescu, I., M. De Batist, G. Lericolais, H. Nouzé, J. Poort, N. Panin, W. Versteeg, and H. Gillet,
803 2006, Multiple bottom-simulating reflections in the Black Sea: Potential proxies of past
804 climate conditions: Marine Geology, v. 227, no. 3–4, p. 163–176,
805 doi:10.1016/j.margeo.2005.12.006.
806 Popov, Y. A., D. F. C. Pribnow, J. H. Sass, C. F. Williams, and H. Burkhardt, 1999,
807 Characterization of rock thermal conductivity by high-resolution optical scanning:
808 Geothermics, v. 28, no. 2, p. 253–276, doi:10.1016/S0375-6505(99)00007-3.
809 Popov, Y., V. Tertychnyi, R. Romushkevich, D. Korobkov, and J. Pohl, 2003, Interrelations
810 Between Thermal Conductivity and Other Physical Properties of Rocks: Experimental
811 Data: Pure and Applied Geophysics, v. 160, no. 5, p. 1137–1161,
812 doi:10.1007/PL00012565.
813 Pribnow, D. F. C., M. Kinoshita, and C. . Stein, 2000, Thermal data collection and heat flow
814 recalculations for ODP Legs 101-180: 1–25 p.
815 Priyanto, B., 2018, Heat Flow Estimation from BSR: An Example from the Aru Region, Offshore
816 West Papua, Eastern Indonesia, *in* Proc. Indonesian petrol. Assoc., 39th Ann. Conv.:
817 Indonesian Petroleum Association (IPA), p. 11, doi:10.29118/IPA.0.15.G.267.
818 Putuhena, H., A. M. W. Newton, J. Cartwright, and M. Huuse, 2021, Middle to late Pleistocene

palaeoceanography inferred from ridge-furrow structures on the continental slope offshore Angola: Marine Geology, v. 439, no. July, p. 106562, doi:10.1016/j.margeo.2021.106562.

Rochelle-Bates, N., M. Huuse, S. Schröder, and G. Pritchard, 2017, Seismic Characterisation of "Prospect B": A Possible Carbonate Build-Up From the Late Syn-Rift (Barremian) of the Lüderitz Basin, Namibia, *in* AAPG Annual Convention and Exhibition.

Ruppel, C. D., and J. D. Kessler, 2017, The interaction of climate change and methane hydrates: Reviews of Geophysics, v. 55, no. 1, p. 126–168, doi:10.1002/2016RG000534.

Samakinde, C. A., J. M. van Bever Donker, R. Durrheim, and M. Manzi, 2021, Hydrocarbon Generation and Migration From Barremian – Aptian Source Rocks, Northern Orange Basin, Offshore Western South Africa: a 3D Numerical Modelling Study: Journal of Petroleum Geology, v. 44, no. 2, p. 187–208, doi:10.1111/jpg.12785.

Sarkar, A. D., 2020, Reflection Seismic Thermometry: University of Manchester, 333 p., doi:10.31237/osf.io/fk7pb.

Sarkar, A. D., and M. Huuse, 2022, Reflection seismic thermometry: Basin Research, v. 34, no. 1, p. 3–24, doi:10.1111/bre.12608.

Schicks, J. M., 2018, Gas Hydrates: Formation, Structures, and Properties, *in* H. Wilkes, ed., Hydrocarbons, Oils and Lipids: Diversity, Origin, Chemistry and Fate. Handbook of Hydrocarbon and Lipid Microbiology: Springer, Cham, p. 81–95, doi:doi.org/10.1007/978-3-319-54529-5_2-1.

Schmidt, S., 2004, The Petroleum Potential of the Passive Continental Margin of South-Western Africa – A Basin Modelling Study: Unpublished PhD dissertation, Fakultät für Georessourcen und Materialtechnik der Rheinisch-Westfälischen Technischen Hochschule Aachen, Germany., 182 p.

Sclater, J. G., C. Jaupart, and D. Galson, 1980, The heat flow through oceanic and continental crust and the heat loss of the Earth: Reviews of Geophysics, v. 18, no. 1, p. 269–311, doi:10.1029/RG018i001p00269.

Serié, C., M. Huuse, N. H. Schødt, J. M. Brooks, and A. Williams, 2017, Subsurface fluid flow in the deep-water Kwanza Basin, offshore Angola: Basin Research, v. 29, no. 2, p. 149–179, doi:10.1111/bre.12169.

Shankar, U., and M. Riedel, 2013, Heat flow and gas hydrate saturation estimates from Andaman Sea, India: Marine and Petroleum Geology, v. 43, p. 434–449, doi:10.1016/j.marpetgeo.2012.12.004.

Shipley, T. H., and M. H. Houston, 1979, Seismic Evidence for Widespread Possible Gas Hydrate Horizons on Continental Slopes and Rises: AAPG Bulletin, v. 63, no. 12, p. 2204–2213, doi:10.1306/2F91890A-16CE-11D7-8645000102C1865D.

Sloan, E. D., S. Subramanian, P. N. Matthews, J. P. Lederhos, and A. A. Khokhar, 1998, Quantifying Hydrate Formation and Kinetic Inhibition: Industrial & Engineering Chemistry Research, v. 37, no. 8, p. 3124–3132, doi:10.1021/ie970902h.

Van Der Spuy, D., 2003, Aptian source rocks in some South African Cretaceous basins: Geological Society, London, Special Publications, v. 207, no. 1, p. 185–202, doi:10.1144/GSL.SP.2003.207.10.

Stoll, R. D., and G. M. Bryan, 1979, Physical properties of sediments containing gas hydrates: Journal of Geophysical Research, v. 84, no. B4, p. 1629–1634, doi:10.1029/JB084iB04p01629.

Thompson, K. F. ., 1979, Light hydrocarbons in subsurface sediments: Geochimica et Cosmochimica Acta, v. 43, no. 5, p. 657–672, doi:10.1016/0016-7037(79)90251-5.

Tissot, B. P., R. Pelet, and P. H. Ungerer, 1987, Thermal History of Sedimentary Basins, Maturation Indices, and Kinetics of Oil and Gas Generation: AAPG Bulletin, v. 71, no. 12, p. 1445–1466, doi:10.1306/703C80E7-1707-11D7-8645000102C1865D.

Torsvik, T. H., S. Rousse, C. Labails, and M. A. Smethurst, 2009, A new scheme for the opening of the South Atlantic Ocean and the dissection of an Aptian salt basin: Geophysical Journal International, v. 177, no. 3, p. 1315–1333, doi:10.1111/j.1365-246X.2009.04137.x.

Waite, W. F. et al., 2009, Physical properties of hydrate-bearing sediments: Reviews of Geophysics, v. 47, no. 4, p. RG4003, doi:10.1029/2008RG000279.

Wanke, A. W., and R. Toirac-proenza, 2018, Seismic Architecture of Outer Shelf Canyon Segments in the Lüderitz Basin, Offshore Namibia, *in* 2018 AAPG International Conference and Exhibition: doi:10.1306/11222Wanke2019.

Wefer, G., W. H. Berger, and C. Richter, 1998, Site 1084, *in* G. Wefer, W. H. Berger, and C. Richter, eds., Proceedings of the Ocean Drilling Program 175 Initial Reports: Ocean Drilling Program, p. 339–384, doi:10.2973/odp.proc.ir.175.112.1998.

Wood, W. T., and C. Ruppel, 2000, Seismic and thermal investigations of the Blake Ridge gas hydrate area: A synthesis, *in* C. K. Paull, R. Matusmoto, P. J. Wallace, and W. P. Dillon, eds., Proceedings of the Ocean Drilling Program: Scientific Results: p. 253–264, doi:10.2973/odp.proc.sr.164.203.2000.

Yamano, M., S. Uyeda, Y. Aoki, and T. H. Shipley, 1982, Estimates of heat flow derived from gas hydrates: Geology, v. 10, no. 7, p. 339, doi:10.1130/0091-7613(1982)10<339:EOHFDF>2.0.CO;2.

Zamora, M., D. Vo-Thanh, G. Bienfait, and J. P. Poirier, 1993, An empirical relationship between thermal conductivity and elastic wave velocities in sandstone: Geophysical Research Letters, v. 20, no. 16, p. 1679–1682, doi:10.1029/92GL02460.

Figure captions

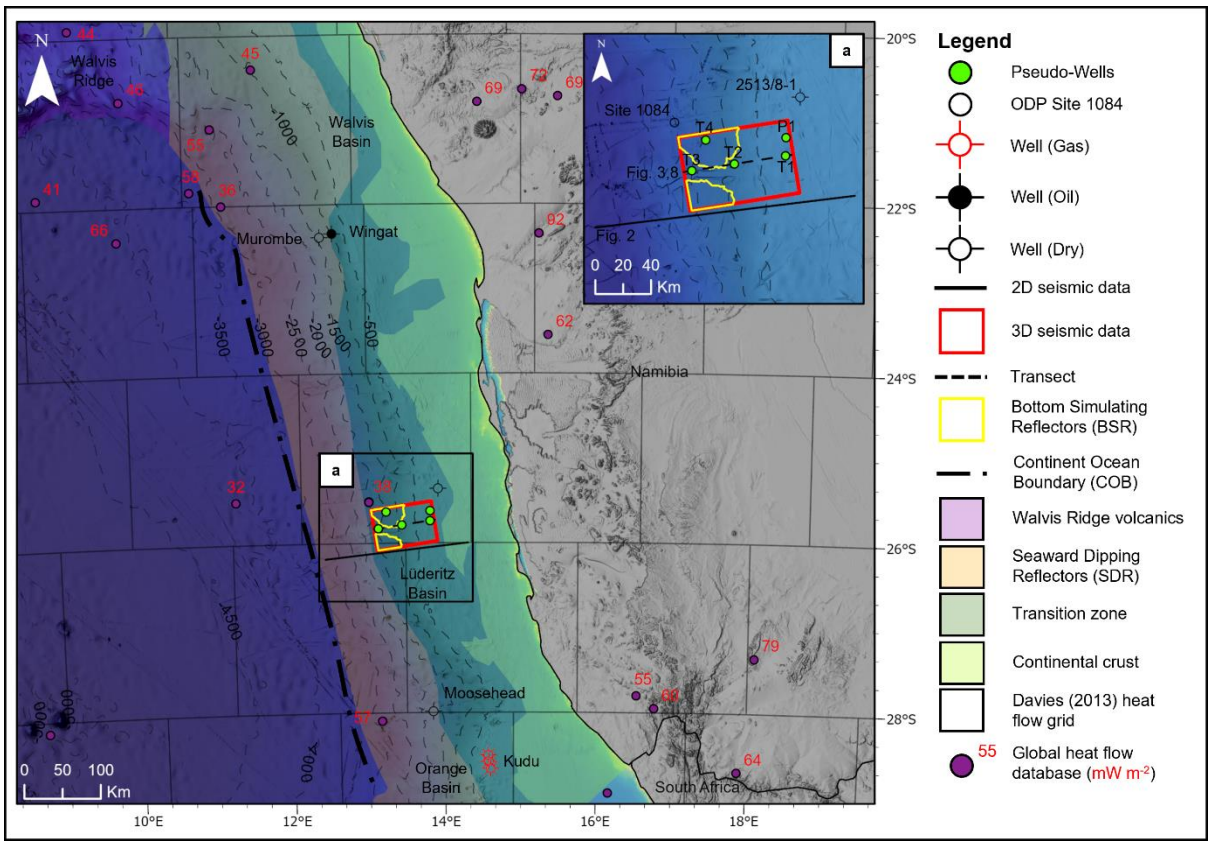

Figure 1: Location map displaying Lüderitz Basin area of interest with available seismic data, using UTM Zone 33 S projection. Key geological, structural and bathymetric features offshore Namibia are highlighted (contour intervals of 500 m [~1640 ft]), adapted from (Bray et al., 1998; Gladczenko et al., 1998; Becker et al., 2009). (a) Inset map displaying extent of seismic data available, mapped BSRs, modelled pseudo-wells and transects along which modelling has been conducted. Example open source global heat flow databases are shown in the form of borehole data (Gosnold and Panda, 2002) and Davies (2013) heat flow grid. Regional exploration wells in neighbouring Walvis & Orange Basins are shown for context.

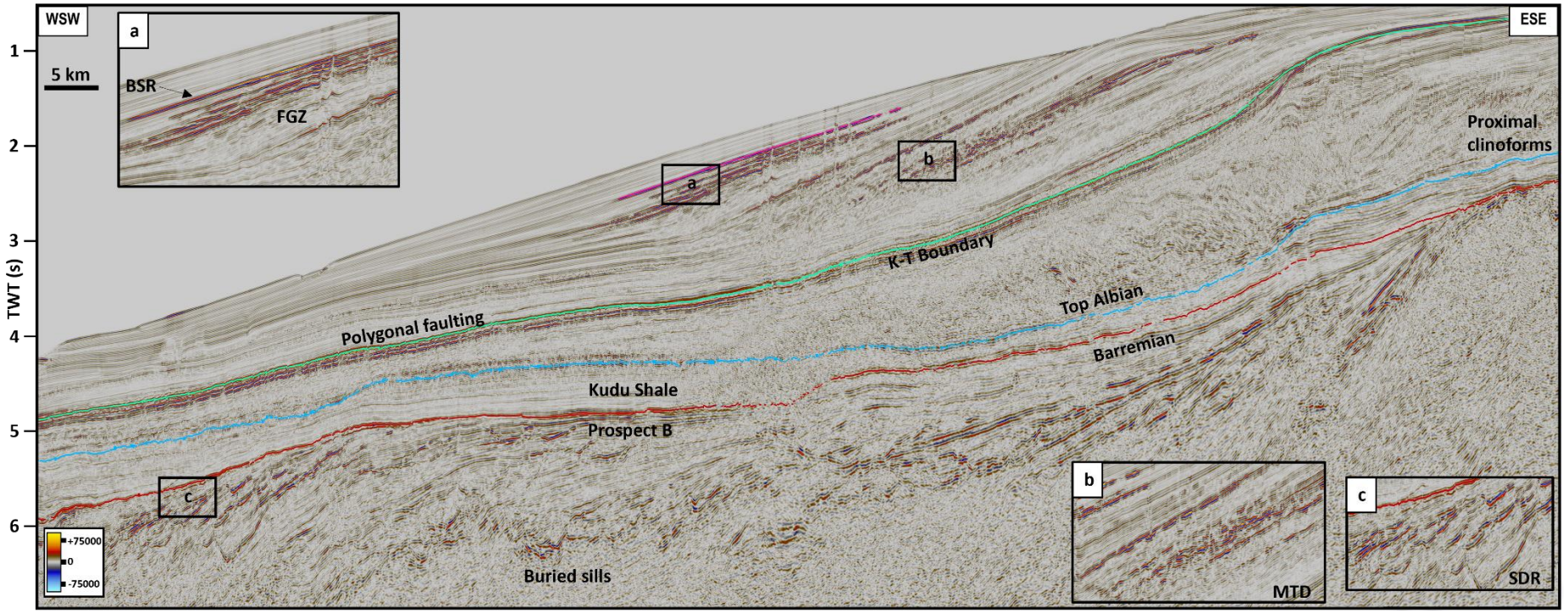

Figure 2: Stratigraphic dip (WSW-ENE) transect displaying two-way travel time (TWT) seismic reflection structure in the Lüderitz Basin. Features visible include clinoforms in near shore section, with (a) BSR, free gas zone (FGZ) below it highlighted by bright reflections (associated with gas) and mass transport features in Tertiary section. (b) Close up of shallow Cenozoic sediments displaying mass transport deposit (MTD) complexes. Cretaceous – Tertiary (K-T) boundary is marked by intense polygonal faulting. In the deeper Mesozoic section, intrusive sills are observable beneath a mounded platform like structure (speculated to be a Barremian carbonate reef) (Rochelle-Bates et al., 2017) overlain by Aptian age "Kudu Shale" source rock interval. (c) Close up of seaward dipping reflectors (SDRs) at depth in the distal section 2D seismic line (Fig. 1a).

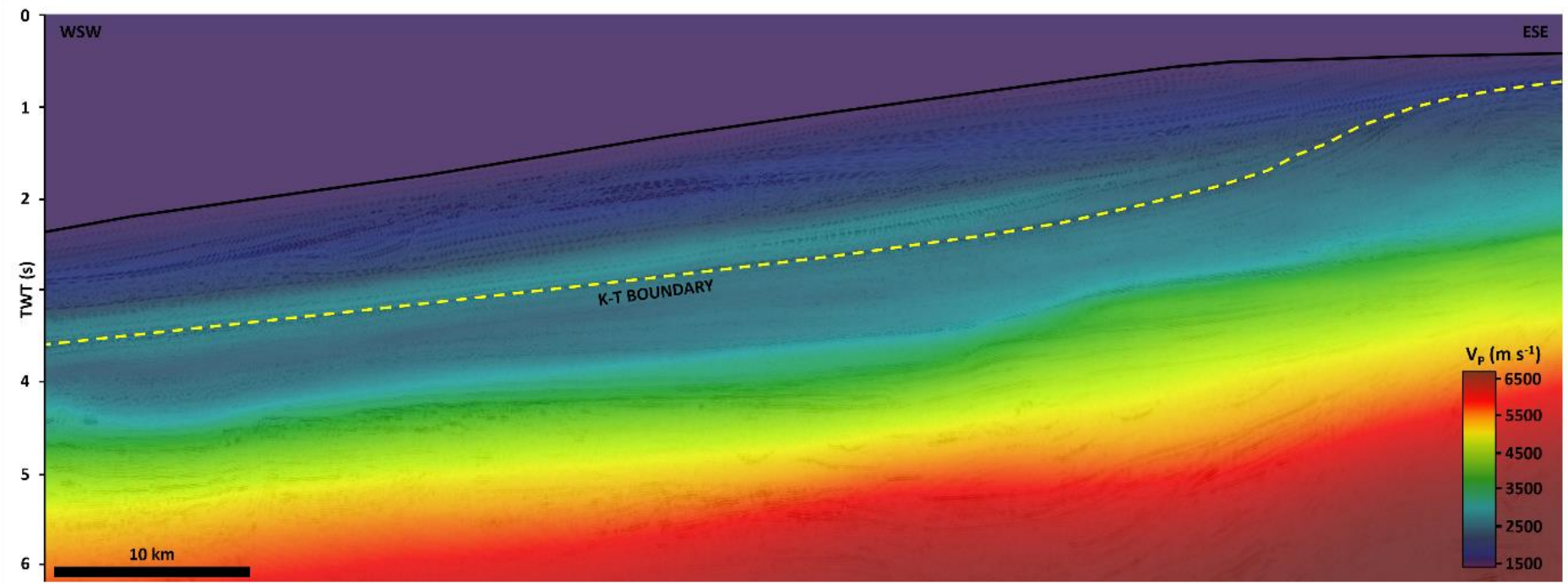

Figure 3: WSE-ENE transect (Fig. 1a) of seismic reflection volume in time domain overlain with interval velocities and K-T boundary highlighted. Velocities near seabed (indicated by the black line) are low (close to water, i.e. 1.5 km/s). Overall deepwater Tertiary section is characterised by low velocities. Velocity inversion seen near K-T boundary (yellow dashed line). K-T = Cretaceous-Tertiary.

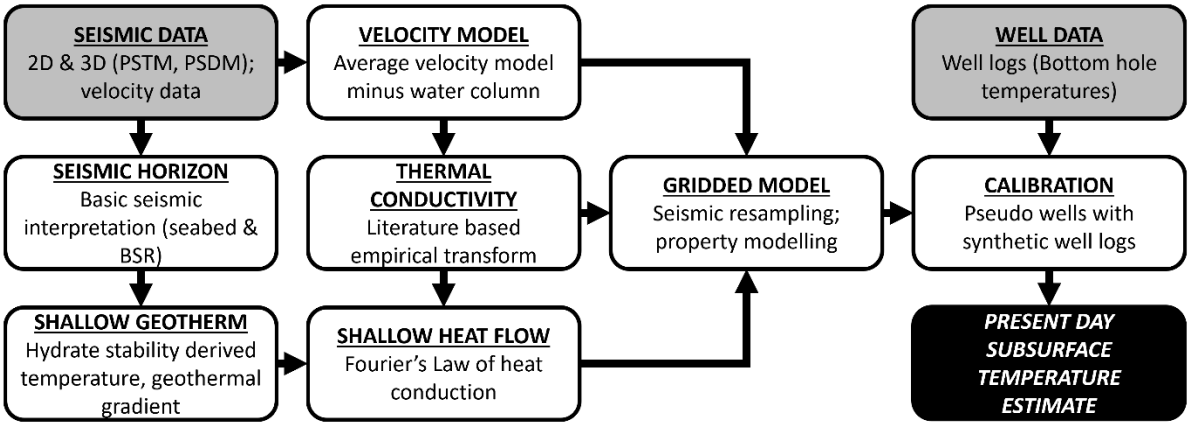

Figure 4: Schematic summary of the steps involved as part of the reflection seismic thermometry methodology used in this study (adapted from (Sarkar, 2020). PSTM = Post Stack Time Migrated; PSDM = Post Stack Depth Migrated; BSR = Bottom Simulating Reflector.

Figure 5: Empirical velocity to thermal conductivity transform utilising experimental datasets from published literature. These measurements are made on samples in laboratory conditions and represent a wide range of lithologies. Furthermore, only results from wet sample measurements are displayed, as the transform will be applied in the shallow subsurface where there is very likely to be fluid fill (for example the GHSZ). Measurements were made using transient method (using optical scanning equipment). GHSZ = Gas hydrate stability zone.

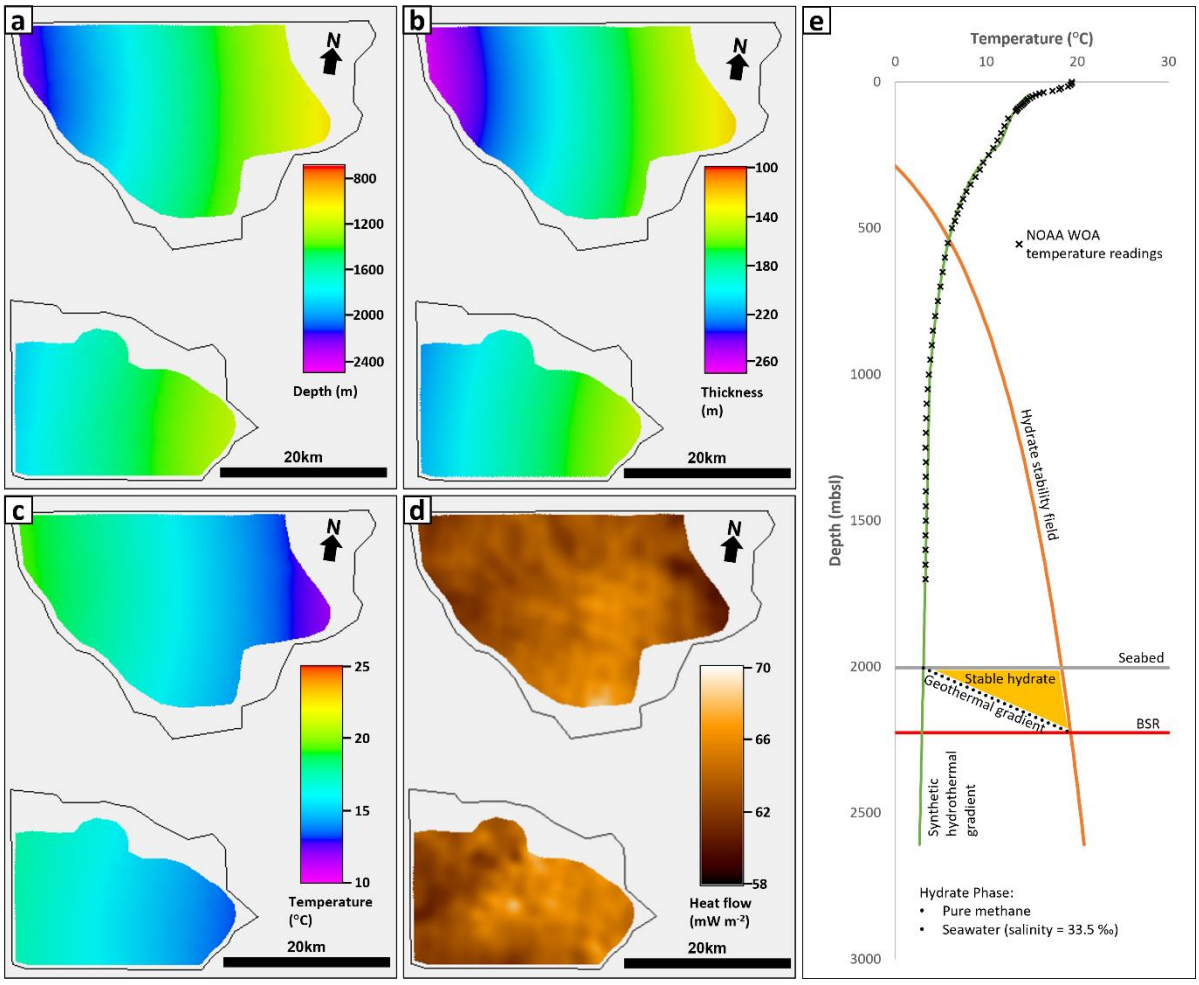

Figure 6: BSR attributes (a – depth; b – GHSZ thickness; c – temperature at base of GHSZ; & e – heat flow) are displayed for high confidence area only, with black polygon representing whole BSR interpretation on seismic. (d) Hydrate stability diagram for a pure methane-seawater system, used to compute temperature at the phase boundary (Fig. 6c). A synthetic hydrothermal gradient is shown, computed using the annualised mean temperature data points from the 1 degree resolution dataset of the WOA (Locarnini et al., 2013). The hydrate stability zone has an average thickness of 184 m (~604 ft) as observed within the study area (Fig. 6b). The cumulative area of both the mapped BSRs is $0.941*10^9$ m^2 ($\sim 1.01*10^{10}$ ft^2). Assuming all the sediment above the BSRs contain gas hydrate, a typical hydrate saturation of 10 % (Waite et al., 2009) would yield a potential methane hydrate volume of $1.73*10^{10}$ m^3 ($\sim 6.11*10^{11}$ ft^3). BSR = Bottom Simulating Reflector; GHSZ = Gas Hydrate Stability Zone; WOA = World Ocean Atlas.

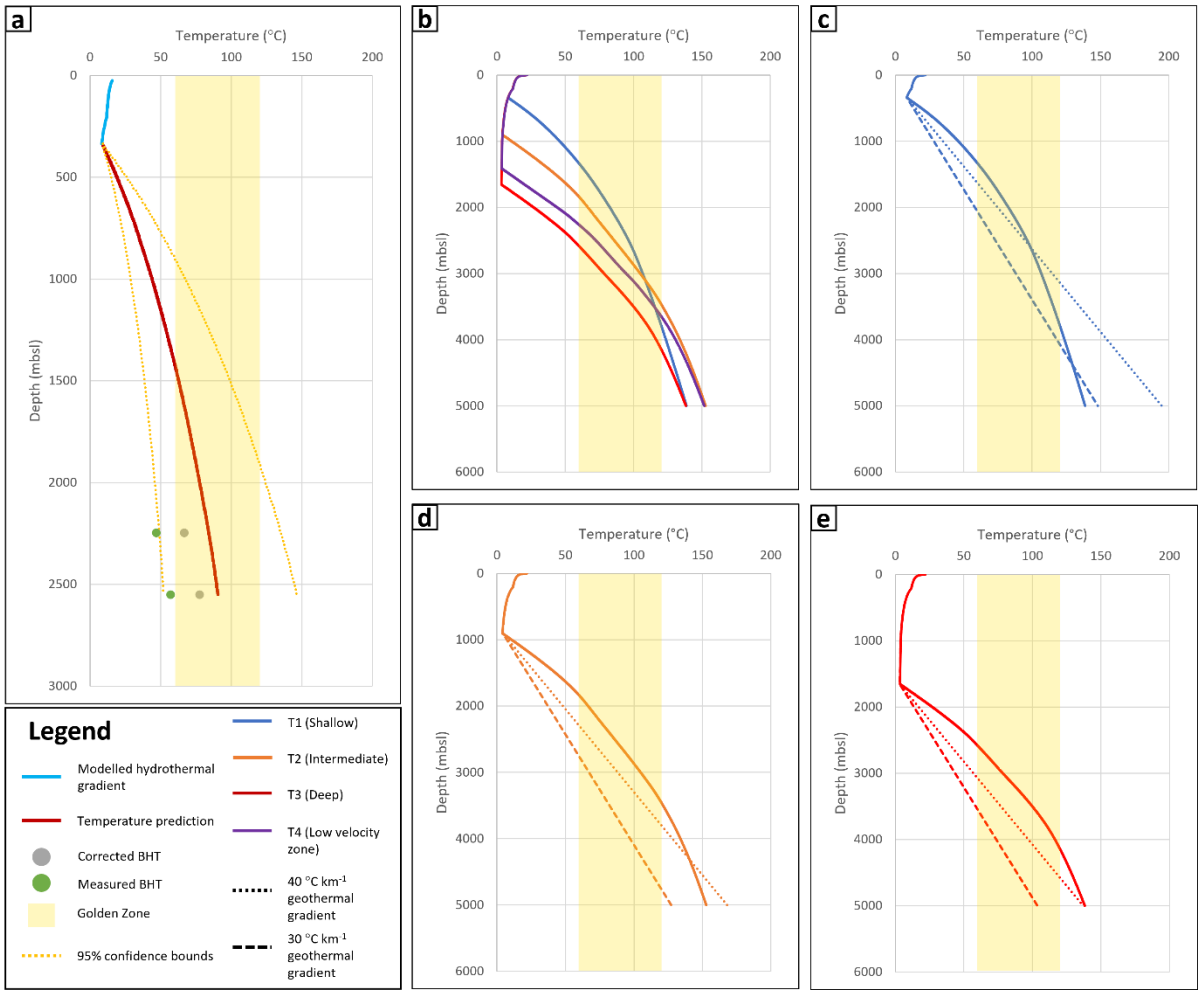

Figure 7: Modelled temperature for 2513/8-1 against measured and corrected borehole temperatures, with Golden Zone interval overlain for reference. (a) Thermal profile for pseudo-well P1 simulating 2513/8-1 with corrected and uncorrected BHT readings. 95% confidence upper and lower bounds are also displayed. (b) Thermal profile for pseudo-wells T1-T4. (c) T1 shallow water thermal profile with modelled linear geothermal gradients. (d) T2 intermediate water depth thermal profile with modelled linear geothermal gradients. (e) T3 deep water thermal profile with modelled linear geothermal gradients. (c-e) Modelling subsurface temperature with typical linear geothermal gradients highlights the variability in depth expected for the Golden Zone. BHT = Bottom hole temperature.

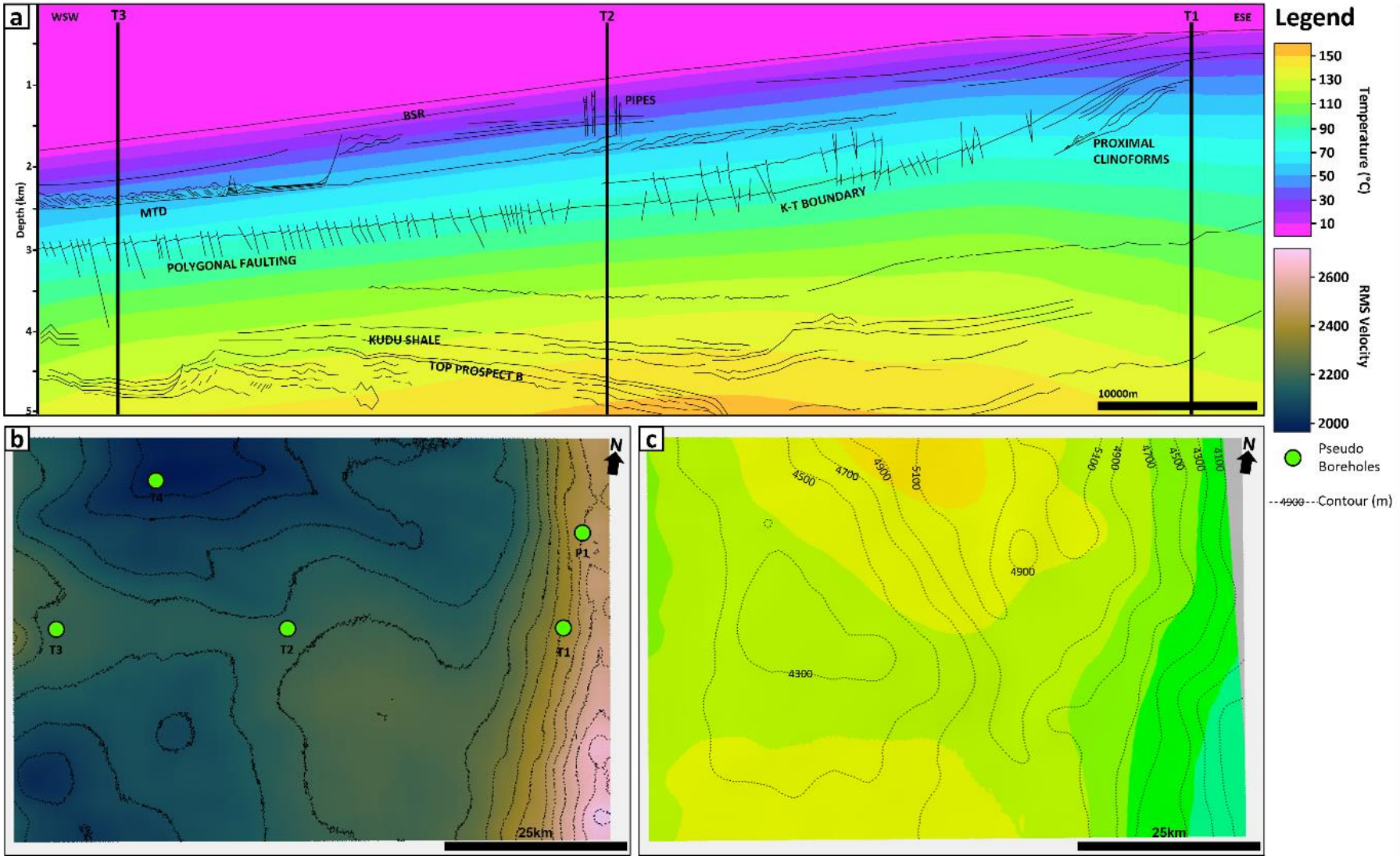
a
WSW
T3
T2
T1
ESE
Depth (km)
BSR
PIPES
MTD
POLYGONAL FAULTING
K-T BOUNDARY
PROXIMAL CLINOFORMS
KUDU SHALE
TOP PROSPECT B
10000m
b
N
T4
P1
T3
T2
T1
25km
c
N
4500
4700
4900
5100
5300
4900
4700
4500
4300
4100
4900
4300
25km
Legend
150
130
110
90
70
50
30
10
Temperature (°C)
2600
2400
2200
2000
RMS Velocity
Pseudo Boreholes
4900
Contour (m)

955

Figure 8: (a) Depth profile of temperature predicted from reflection seismic thermometry. Pseudo-wells corresponding to shallow, intermediate, and deep water are marked. (b) RMS velocity extraction of interval velocities (for interval up to 2 s below seabed) highlighting the zone of low velocities encountered below, in particular, the Northern BSR. Pseudo-well T4 is placed to illustrate this. (c) Temperature prediction from the model mapped across the base of the Aptian source rock above the mounded structure referred to as Prospect B (Fig. 2c). The thermal model produced was used to interrogate the predicted present-day temperature for the base of the source rock interval as shown in Fig. 2c. The temperature ranged between 93.2 – 157.2 °C [200 – 315 °F] for a depth range of 3400 – 5400 mbsl [~11155 – 17717 ftbsl]. Scientific colour bar templates based on (Crameri et al., 2020). RMS = Root Mean Squared; BSR = Bottom Simulating Reflector; mbsl = metres below sea level; ftbsl = feet below sea level.

Tables

Table 1: Parameters for BSR derived heat flow bounds, with the hydrate phase, pressure gradient and seabed temperature kept unchanged. BSR = Bottom Simulating Reflector.

Sediment velocity (m s^{-1})	Hydrate phase	Thermal conductivity (W m^{-1} K^{-1})	Pressure conditions	Seabed temperature	Heat flow bound
Minimum	Pure methane & seawater	Minimum	Hydrostatic	Modelled hydrothermal gradient	Minimum
Maximum	Pure methane & seawater	Maximum	Hydrostatic	Modelled hydrothermal gradient	Maximum